In-situ evolution of active layers on commercial stainless steel for stable water splitting

Yanhong Lyu[a], Ruilun Wang[a], Li Tao[a], Yuqin Zou[a,*], Huaijuan Zhou[b], Tingting Liu[a], Yangyang Zhou[a], Jia Huo[a], San Ping Jiang[c], Jianyun Zheng[a,*], Shuangyin Wang[a,*]

[a] State Key Laboratory of Chem/Bio-Sensing and Chemometrics, College of Chemistry and Chemical Engineering, Hunan University, Changsha 410082, Hunan, China
[b] State Key Laboratory of High Performance Ceramics and Superfine Microstructure, Shanghai Institute of Ceramics, Chinese Academy of Sciences, Shanghai 200050, China
[c] Western Australian School of Mines: Minerals, Energy and Chemical Engineering and Fuels and Energy Technology Institute, Curtin University, Perth, Western Australia 6102, Australia

ARTICLE INFO

ABSTRACT

Efforts to explore earth-abundant, non-precious electrocatalyst, especially commercial stainless steel, to replace precious-metal-based catalyst have attracted increasing interest in renewable energy research. Herein, we design a facile and simple route to fabricate highly efficient 316L-type stainless steel-based electrocatalysts for water splitting by CH_4 plasma. After CH_4 plasma treatment, the amorphous carbon layer and the graphene encapsulated Fe_3C nanoparticles are observed on the surface of stainless steel, which play the roles of active sites and protective layer for simultaneously providing an acceptable hydrogen evolution reaction (HER) and excellent oxygen evolution reaction (OER). The optimized stainless steel-based electrocatalyst exhibits an over-potential of only 290 mV at 10 mA cm^{-2} and possesses outstanding kinetics (the Tafel slope of 38 mV dec^{-1}) for OER in the 1.0 M KOH aqueous solution. We anticipate that the operating strategy of our system may aid the development of commercial non-precious productions as the efficient electrocatalysts for energy storage and conversion.

1. Introduction

Electrochemical water splitting as a promising friendly environmental technology for the future hydrogen-based economy has received considerable attentions [1–5]. As for the two half reactions involving in water splitting: oxygen evolution reaction (OER) and hydrogen evolution reaction (HER), OER is a determinant step due to the multiple electron and proton transfer process [6,7]. Although noble metals or their compounds, such as Pt and RuO_2, are famous for their comparatively low overpotential as HER and OER electrocatalysts, the high cost and scarcity of noble metals severely limit their wide used in the electrochemical water splitting [8,9]. Many efforts have been made to develop low-cost and earth abundant water-splitting electrocatalyst [10–14].

Iron is one of most abundant elements on earth, and recently there is an obvious excess capacity in the global steel industry, especially in China. Applying the commercial stainless steels as the efficient electrocatalysts for water splitting is a challenging and interesting way to solve the issues [15–19]. The stainless steel contains rich transition metal (TM) elements like iron and nickel, which usually are active centers in the electrochemical reactions. In fact, the original stainless steel still shows sluggish water-splitting performance, in particular OER. Currently, the 304-type stainless steels are employed as the electrocatalyst for OER because of low cost. In the previous work, some groups have used the original or treated 304 type stainless steels as the electrocatalysts to obtain a good performance for water splitting [15–18]. In comparison to 304-type stainless steels, 316L-type stainless steels (denotes as SS) has more stable and corrosion-resistant structure, even under positive applied bias, implying the potential application for the electrocatalyst. But, the surface of SS usually shows relatively chemical inertness, and thus is difficult to be modified as an efficient electrocatalyst for water splitting. Apparently, it is highly desirable to develop a facile and feasible route to achieve an efficient SS-based electrocatalyst for water splitting.

Due to surface chemical inertness, the water-splitting performance of modified SS by single traditional method, such as annealing, is seldom successful. In addition, in the previous reports, the new treatment technologies like plasma treatment were just employed to

modified the mechanical properties of SS [20,21], but the effect of plasma treatment on the electrocatalytic performance of SS is absent. However, developing an efficient route to improve the electrocatalytic performance of SS and understanding its working mechanism are necessary and significant. In this respect, we utilize a facile route including three steps to construct an excellent SS-based electrocatalyst: (i) etched by hydrochloric acid, (ii) oxidized by thermal treatment, and (iii) carbonized by CH_4 plasma treatment. Among them, the etching process gives rise to the formation of rough surface for SS and the elimination of passivation materials like chromium oxide, which can be regarded as the activation step for developing the next steps. Subsequently, the particles of transition metal oxide (TMO) (e.g. Fe_2O_3) are created from the surface of SS via thermal treatment in air and are employed as the source of TMs to facilitate the carbonizing process. The CH_4 plasma treatment is the dominant step in the total process of surface modification for SS, which could produce the transition metal carbides (TMCs) on the surface of SS. In addition, the TMs encapsulated by carbon can prevent the corrosion of TMs materials in the electrolyte and efficiently promote the catalytic reaction [22–25].

In this study, we successfully realized the in-situ evolution of active layers from the SS surface, and demonstrated a novel and facile route to achieve the SS-based electrodes with the amorphous carbon (a-C) layer and graphene encapsulated Fe_3C nanoparticles ($Fe_3C@G$). The modified SS electrodes showed a good water-splitting performance, especially OER, which achieves a Tafel slope of 38 mV dec^{-1} and overpotential of 290 mV for OER. We investigated the effect of CH_4 plasma treatment on the composition and structure of the SS-based surface and understood the relationship between these changes and water-splitting behaviors. Our understanding of the SS-based electrode with a-C layer and $Fe_3C@G$ resulted in the development of a new strategy to optimize both the structure and composition of the SS surface, enabling efficient utilization of surface-forming active sites (such as Fe_3C) for electrocatalytic water splitting.

2. Experimental section

2.1. Sample preparation

2.1.1. Preparation of etched SS (ESS)

Firstly, the commercial 316L type SS (2.0 cm * 4.0 cm, Tianhong Stainless Steel Co., Ltd) were cleaned ultrasonically in distilled water and absolute ethanol for 15 min, respectively. Then, the SS were etched ultrasonically in 3 M HCl for 30 min. After erosion process, the samples were thoroughly washed with distilled water to remove the impurities from the source solution, and then were dried in 24 h at 60 ℃ in vacuum. The obtained samples were denoted as ESS.

2.1.2. Preparation of oxidized ESS (OESS)

The as-prepared ESS samples were annealed at 500 ℃ for 60 min under air in muffle roaster at heating rate of 10 ℃ min^{-1}. The obtained samples were denoted as OESS.

2.1.3. Preparation of OESS with CH_4 plasma treatment (OESSC)

The CH_4 plasma treatment was carried out by a homemade plasma generator with a tube furnace and a commercial 13.56 MHz RF source. Before the plasma treatment, the as-prepared OESS samples were placed at the central of tube furnace and heated to 300 ℃ at a heating rate of 10 ℃ min^{-1} under CH_4 flow (4 sccm). For the plasma treatment, the RF power was 200 W, and the treatment time is 20 min. The obtained samples were denoted as OESSC. For comparison, other samples were prepared at the different temperature (room temperature, 300℃, 400 ℃ and 500℃), RF power (100 W, 200 W and 300 W), and treatment time (10 min, 20 min and 30 min), respectively. In this work, the OESSC sample was fabricated at condition of 20 min, 300 ℃ and 300 W for CH_4 plasma treatment, unless the fabrication conditions state otherwise.

2.1.4. Preparation of other samples

The SS was directly oxidized (labeled as OSS) via annealing in air, and then was carbonized (labeled as OSSC) with CH_4 plasma treatment. In addition, the carbonized SS by CH_4 plasma treatment was named as SSC, and the ESS treated by CH_4 plasma treatment is defined as ESSC. All of the treatment conditions are identical to that implemented in OESSC.

2.2. Sample characterization

To investigate the crystalline structure of samples, a Rigaku diffractometer (Rigaku Ultima IV) using Cu Kα radiation (λ = 0.15406 nm) was employed to performing 2θ X-ray diffraction (XRD) scans with the grazing angle of 1° at the scan rate of 2° min^{-1}. The chemical composition of samples was analyzed by X-ray photoelectron spectroscopy (XPS) technology, which was performed on an ESCALAB 250Xi X-ray photoelectron spectrometer using Mg as the excitation source. All binding energies were referenced to the C1s peak (284.8 eV) arising from adventitious carbon. The morphology and microstructure of samples were investigated by field emission scanning electron microscope (FESEM, Hitachi, S-4800). The composition was tested by line-scanning energy dispersive x-ray spectroscopy (EDS) attached FESEM. The Raman spectra were collected on a Raman Spectrometer (Labram-010) using 532 nm laser. In situ Raman spectra were obtained on a Micro-Raman Spectroscopy System (DXR, ThermoFisher Scientific) with an excitation laser wavelength of 780 nm and a power of ca. 5 Mw. A 50× long-working-length objective was used to focus the laser light on the samples. Aiming to further determine the microstructure of samples, high-resolution transmission electron microscopy (HRTEM, Tecnai G2 F20 S—Twin) was employed to observe the surface and cross section of samples. The surface area was measured by nitrogen adsorption-desorption isotherms at 77 K with a JW-BK200C system (JWGB SCI & TECH). Hydrogen Temperature Programmed Reduction (H_2 - TPR) was performed on a micromeritics instrument (AutoChem1 II 2920). The catalyst debris (100 mg) were placed in a U-shaped quartz reactor, pre-treated in flowing Ar (50 mL/ min) for 0.5 h at 300 ℃, and followed by cooling to room temperature. The temperature was then raised from room temperature to 1000 ℃ at a rate of 10 ℃/min under a 10% H_2 /Ar flow (50 mL/min). A thermal conductivity detector was employed to monitor the H_2 consumption. The surface work function of the samples was analyzed by ultraviolet photoelectron spectroscopy (UPS) (ThermoFisher ESCALAB 250Xi).

2.3. Electrochemical measurements

All the electrochemical measurements including CV and linear sweep voltammetry (LSV) were measured in 1 M KOH electrolyte by an electrochemical workstation (CHI 600, CH instrument) with a three-electrode cell, using carbon rod as counter electrode and saturated calomel electrode (SCE) as reference electrode. The working electrode was as-prepared self-supported sample, as mentioned above. The scan rate of LSV was set to 5 mV s^{-1}. All polarization curves in this work were corrected by iR correction due to the ohmic resistance of the solution. Potentials were referenced to a reversible hydrogen electrode (RHE) by yielded the equation: $E_{RHE} = E_{SCE} + 1.05$ V. The electrochemically active surface CVs measurements of working electrodes were carried out for two cycles between 1.1 and 1.25 V vs. RHE, and the scan rates of 2, 4, 6, 8 and 10 mV. The C_{dl} was estimated from plotting the ΔJ at different potentials against the scan rates. The EIS tests of samples were performed by an Autoab electrochemical workstation (Autolab PGSTAT302 N, MetrohmAutolab BV, Netherlands) at a potential of 1.54 V vs. RHE over the frequency range from 1 MHz to 0.1 Hz in 1 M KOH. All the catalysts were activated by CV scan until reaching a stable state before testing the catalytic activity.

The O_2 and H_2 gas were detected by Gas Chromatography (GC) System (SP-7820, Lunanruihong Co., Ltd). The GC directly connected to

the electrochemical reaction cell via gas lines. When the i-t measurements were performed at 59 mA cm^{-2}, the evolved gas was recorded at every 20 min. Therefore, the Faradaic efficiency can be calculated as follows,

$$FE_{O_2} = \frac{4 \times 96485 \times n_{o_2}}{Q_{OER}} \quad (1)$$

$$n_{O_2} = \frac{V_{o_2}}{V_m} \quad (2)$$

$$FE_{H_2} = \frac{2 \times 96485 \times n_{H_2}}{Q_{HER}} \quad (3)$$

$$n_{H_2} = \frac{V_{H_2}}{V_m} \quad (4)$$

where the n is molar mass of evolved gas, V is volume of evolved gas obtained by GC, V_m is molar volume 22.4L/mol, and Q the total charge passed through electrode."

The turnover frequency (TOF) is a very important kinetic parameter for OER [26]. TOF shows the intrinsic property of the catalysts, which is important for evaluating the performance of the catalysts. The TOF value was calculated from the equation.

$$TOF = (j \times A)/(4 \times F \times m) \quad (5)$$

where j is the current density at overpotential of 0.29 V for OER, A is the geometry area of the SS mesh electrode, F is the faraday constant (a value of 96485 C mol^{-1}), and m is the number of moles of the active materials calculated by the results of H_2-TPR. All the Fe atoms in the iron oxide of OESS and in the iron carbide of OESSC were assumed to be accessible for catalyzing water splitting.

3. Results and discussion

3.1. Materials characterization

Three fabrication steps of SS-based anodes are illustrated in Fig. 1, including chemical etching, thermal oxidation and plasma carbonizing. The composition of original commercial SS was $Fe_{0.7}Cr_{0.17}Ni_{0.11}Mo_{0.02}$ (Fig. S1). The fresh SS with smooth surface (Fig. S2a) was used as both a current collector and precursor. To create the more activities, the SS samples successively underwent the acid etching (denoted as ESS) and oxidizing progress (denoted as OESS), and a wrinkle and porous surface on the OESS samples was formed (Fig. S2c). After that, the CH$_4$ plasma treatment was conducted to carbonize the OESS (denoted as OESSC) for forming the TMCs or carbon-based materials (Fig. S2h). In this work, the OESSC sample was fabricated by CH$_4$ plasma treatment with the power of 300 W at 300 °C for 20 min, unless the fabrication conditions stated otherwise. As the control experiments, the etched SS (ESS), the oxidized SS (OSS), the carbonized SS (SSC), the etched and carbonized SS (ESSC) and the oxidized and carbonized SS (OSSC) were also fabricated and characterized.

The SEM results show that the plasma treatment can etch the surface of the SS effectively to produce the discontinuous structures, without destroying the SS wires. In comparison to other samples (Fig.

S2), OESSC sample with active layers consisting of the nanoparticles (Fig. 2a and b) exhibited rougher surface than other samples, indicating that the OESSC sample has a higher specific surface area than others. To investigate the crystal structure of SS-based electrodes, X-ray diffraction (XRD) characterizations were shown in Fig. 2c. XRD results reveal that all the samples had the same three peaks at 43.6°, 50.7° and 74.7°, assigning to the austenite phase (PDF card #33-0397). After CH$_4$ plasma treatment, both of the ESSC and OESSC samples displayed the broader and lower peaks than the other samples, implying the possible presence of nanoparticles and amorphous structure in the OESSC sample via various treatments. It is known that amorphous materials are more active than the crystalline one due to the "dangling bonds" in the amorphous phase [27]. Chromium oxide plays a role of extremely strong passivation layer which prevents corrosion of stainless steel, to verify the removing of chromium oxide, XPS technical was applied to analyze the surface composition of SS and ESS. As shown in Fig. S3, after etching, the ratio of Fe/Cr obviously increased from ~3.05 to ~28.14, which indicates that the chromium oxide on the surface is removed. Meanwhile, the micropores were generated on the surface of SS after etching, as shown in the right of Fig. S3. In addition, in the XRD data (Fig. 2c), there is a small peak at around 10° for SS sample, which is not observed for other samples. In fact, according to the PDF retrievals PDF #36-1329, the small peak at around 10° for SS sample is Cr_2O_5. After etching, the peak of Cr_2O_5 is disappeared in ESS, OESS, ESSC and OESSC samples, in line with the XPS data. Further, Raman spectroscopy was used to efficiently identify the structure of the materials, especially carbon. After oxidizing treatment, the Raman modes of iron oxide (Fe_2O_3 and Fe_3O_4) were obviously found in the OESS sample (Fig. 2d). Subsequently, via CH$_4$ plasma treatment, two obvious peaks in the OESSC sample were revealed at ~1320 and ~1590 cm^{-1}, which correspond to the D-band and G-band of carbon, respectively. Due to the pretreatment of oxidizing, the intensity of both D peak and G peak in the OESSC sample is larger than that in the ESSC sample. D-band intensity is proportional to defects level of carbon materials, while G-band intensity is related with a stretching vibration in the plane of sp^2 hybridized carbon atoms [28–31]. The ratio of the D-band and G-band represents the defects in the carbon structure. The I_D/I_G value (1.02) of OESSC sample is higher than that of ESSC sample (1.0), because D-band intensity of OESSC sample shows faster increase than G band intensity, which reflects the increase of defect level in the OESSC sample.

Cross-sectional field-emission scanning electron microscope (FESEM) and transmission electron microscope (TEM) were employed to observe the structure of the samples. The surface of OESSC sample displayed a discrete layering structure (Fig. 3a), which consisted of carbonization layer and oxidation layer from surface to inner in sequence. However, the interface between the carbonization layer and oxidation layer was gradual and blurry. Additionally, the result of EDS line scanning indicates that the OESSC sample was composed of the carbonization layer, oxidation layer and SS bulk, in which the thickness of carbonization layer was ~50 nm (Fig. 3b). It should be noted that a portion of iron and oxygen atoms existed in the carbonization layer. Further analysis on the cross-sectional morphology of OESSC sample
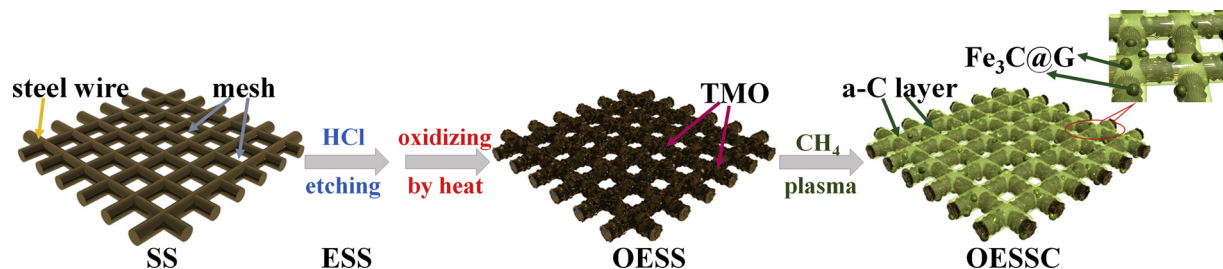

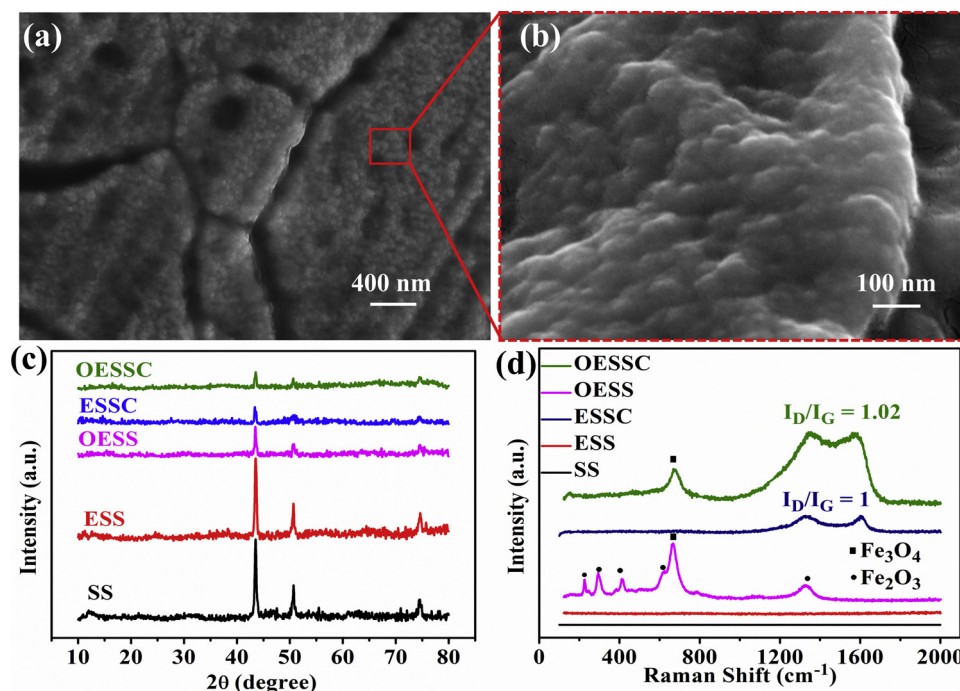**Fig. 1.** Schematic illustration of the fabrication procedure of SS-based electrodes.

Fig. 2. (a) Low magnification images of the surface of OESSC sample. (b) High magnification images corresponding to the marked area in (a). (c) XRD patterns of the SS-based samples. (d) Raman spectra of the SS-based samples.

was then carried out via transmission electron microscopy (TEM). As presented in Fig. 3c, the OESSC sample showed oxidization layer and carbonization layer on the surface. The encapsulated nanoparticles were randomly distributed in the carbonization layer. In addition, the high-resolution TEM (HRTEM) image revealed the nanoparticle and the encapsulating shell with the spacing lattice fringes of ˜0.20 and ˜0.34 nm, which can be indexed as the (031) plane of Fe₃C and the interplanar distance of graphene, respectively. As a result, the Fe₃C nanoparticles encapsulated by several layers of graphene is produced

by CH₄ plasma treatment, as depicted in the right of Fig. 3c. In the previous work [23–25], the core-shell structure (Fe₃C@G) can modulate the electronic state of carbon in the graphene shell and surrounding amorphous carbon matrix by the electron transferred from the encapsulated metal carbide core, which reflects in the increase of sp³ carbon. As expected, the CH₄ plasma treatment can reduce the iron oxide of OESS sample to form iron carbide by the CH₄ gas, and decompose the CH₄ gas into the graphene shells and amorphous carbon layer.
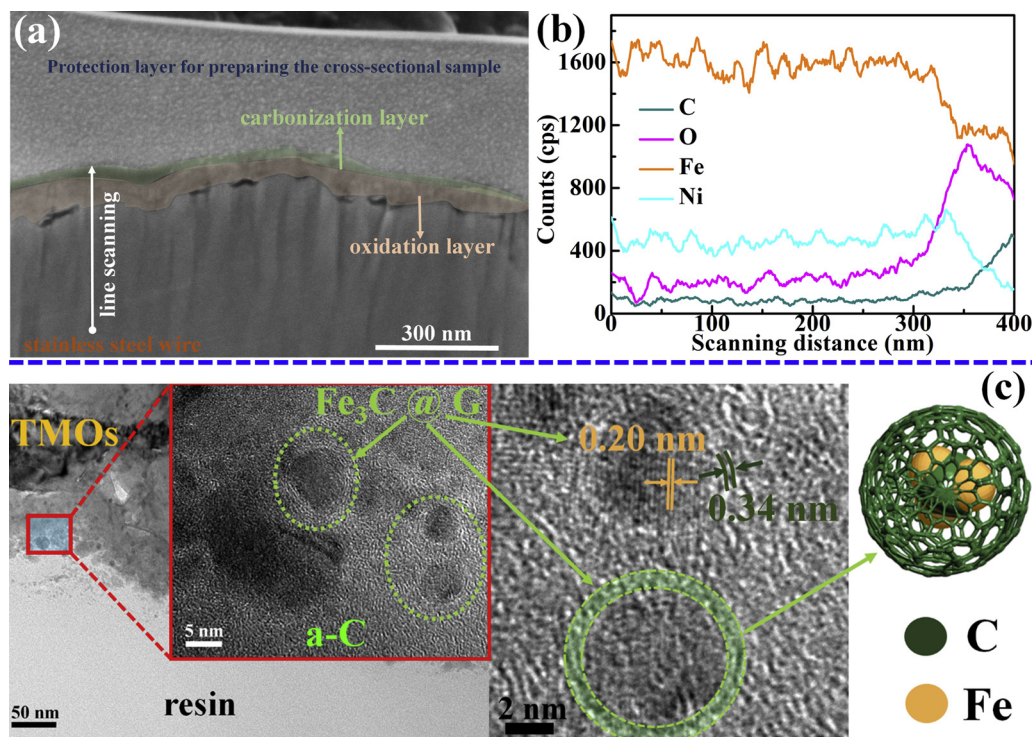

Fig. 3. (a) Cross-sectional FESEM image of OESSC sample. The green region and pink region is carbonization layer and oxidation layer, respectively. (b) EDS line scanning data of OESSC sample. The scanning range is marked by white arrows in the (a). (c) Cross-sectional TEM images of OESSC sample: low magnification (left), corresponding high magnification (middle), and schematic illustration of Fe₃C@G (right) (For interpretation of the references to colour in this figure legend, the reader is referred to the web version of this article).
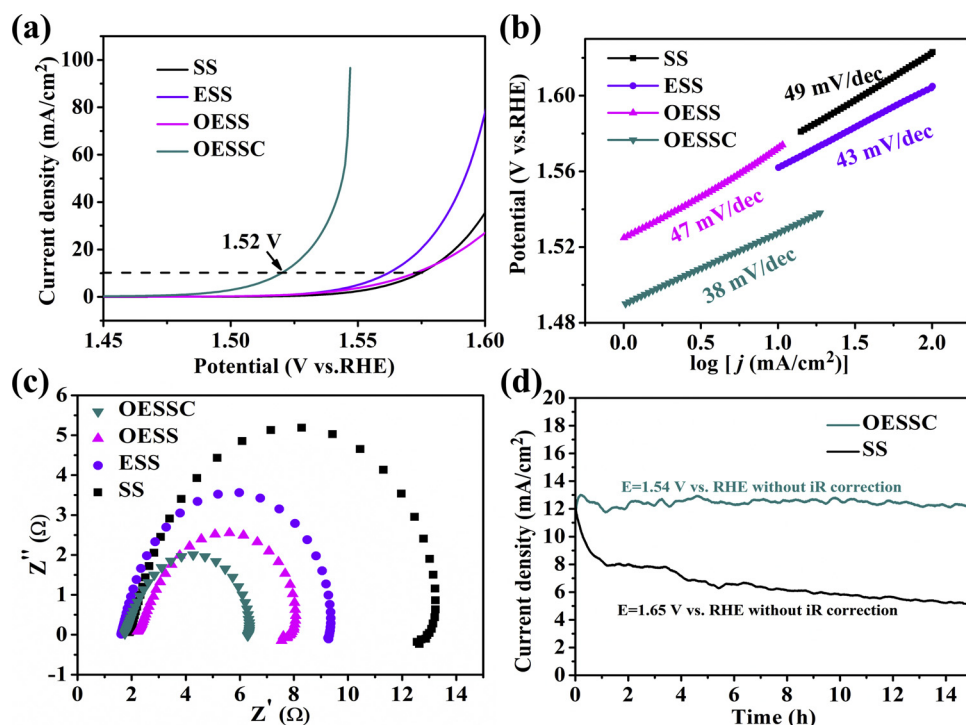
Fig. 4. (a) Polarization curves of SS, ESS, OESS and OESSC samples for OER. (b) Corresponding Tafel plots of the samples. (c) EIS of SS, ESS, OESS and OESSC samples at the potential of 1.54 V vs. RHE. (d) Time-dependent current curves of OESSC and SS samples at initial current density of ~12 mA cm^{-2} under a static potential of 1.54 V and 1.65 V vs. RHE without iR correction for 54,000 s, respectively.

3.2. Electrocatalytic performance

The catalytic activity of the prepared catalysts for OER was assessed in 1.0 M KOH, as shown in Fig. 4. The OESSC sample exhibited a low overpotential of 290 mV at 10 mA cm^{-2}, while the SS samples needed an overpotential of 350 mV. In addition, the samples (like SSC, OSSC and OESSC) treated by CH$_4$ plasma showed better OER performance than that without CH$_4$ plasma treatment (like SS, OSS and OESS) (Fig. S4). In addition, compared to the SSC, ESSC and OSSC samples, the OESSC sample displayed a more efficient OER behavior. To further investigate the effect of CH$_4$ plasma treatment with different working parameters, the OESSC samples were also treated with different power, time and temperature (Figs. S5 and S6). As shown in Fig. S5a, OESSC sample treated by low-power CH$_4$ plasma (100 W) showed a poor OER performance, because the Fe$_3$C@G nanoparticles are hardly formed on the surface by such low-power plasma. Furthermore, when treatment time increases, more Fe$_3$C@G nanoparticles and defects can be generated, resulting in a good electrocatalytic activity (Fig. S5b). In addition, a moderate temperature can promote the reactions of plasma and sample. As shown in Fig. S6, the OESSC sample fabricated at 300 °C shows better electrocatalytic performance than at other temperatures. However, the disorder thermal motion can disturb the moving trajectory of the plasma at exorbitantly high temperature, and thus the plasma treatment is weakened. In this work, OESSC sample shows an optimal OER performance by CH$_4$ plasma treatment at 300 °C. According to these results, the presence, composition, and thickness of carbonization layer affect the electrocatalytic activity of the samples.

The electrocatalytic kinetics of OER was estimated by Tafel slope. In Fig. 4b, the Tafel slope of OESSC sample was calculated to be 38 mV dec^{-1}, lower than the SS (49 mV dec^{-1}), ESS (43 mV dec^{-1}) and OESS (47 mV dec^{-1}). It is observed that the OESSC sample possesses faster catalytic kinetic, and hence the rapid OER rate could be realized. The fast OER kinetics on the OESSC sample was also verified by electrochemical impedance spectroscopy (EIS) analysis (Fig. 4c). The charge transfer resistance at 1.54 V on the OESSC sample was lower than the SS, ESS and OESS samples, which indicates that the OESSC have a much faster electron transfer for OER than the SS, ESS and OESS samples.

To evaluate the stability of the electrocatalysts, long-duration i-t

measurements were carried out. The OESSC and SS samples were applied a constant potential of 1.54 V and 1.65 V vs. RHE without iR correction for 54,000 s, respectively. As shown in Fig. 4d, the initial current density of OESSC and SS samples is ~12 mA cm^{-2}. After 54,000 s in alkaline environment, the current density of OESSC sample exhibited negligible change, while the pristine SS samples dropped down to 5.2 mA cm^{-2}, indicating the excellent stability of OESSC sample for OER. Besides, the stability of ESSC and OESS samples was also evaluated at a constant potential of 1.61 V, respectively (Fig. S7). Even though the surface structure of the ESSC and OESS samples keeps well, their current densities drop down obviously with the increase of the reaction time. After the stability tests, the LSV curve of OESSC sample nearly remained the original state, while the SS degraded obviously (Fig. S8), which also verifies the excellent stability of OESSC sample. The in-situ Raman spectroscopy (Fig. S9) assesses the change in the structure and composition of OESSC sample in 1 M KOH during OER. The results of Raman spectra show that there is no shift and deformation in the carbon peaks when the applied biases are from 1.45 to 1.85 V vs RHE. The surface composition and structure of OESSC sample before and after long-term electrolysis were also analyzed. As shown in Fig. S10a, after i-t measurement, the XPS peak of Fe 2p$_{3/2}$ was slightly shifted to higher binding energy, which indicates that the Fe elements on the OESSC surface can couple with the additional oxygen elements. However, the contents of Fe$_3$C in the total Fe elements still keeps 19.01% after long-duration electrolysis, which approximates the original value (19.89%) before electrolysis. In addition, the morphology of the OESSC sample is basically unchanged before and after electrolysis (Figs. S10b and S10c). The highly durable OESSC sample can be attributed to the structural advantage: the carbon matrix could prevent the degeneration of the structure and the oxidation of the embedded nanoparticles.

The catalytic activity of hydrogen evolution was also estimated in 1 M KOH. As displayed in Fig. 5a, the OESSC showed an enhanced HER activity with a low overpotential of 264 mV at 10 mA cm^{-2}. The EIS analysis (Fig. 5b) reveals that the charge transfer resistance of OESSC sample at -0.25 V vs. RHE was lower than the SS, ESS and OESS samples, implying a faster electron transfer for the OESSC sample. Like OER performance, the HER performance of OESSC sample is also influenced
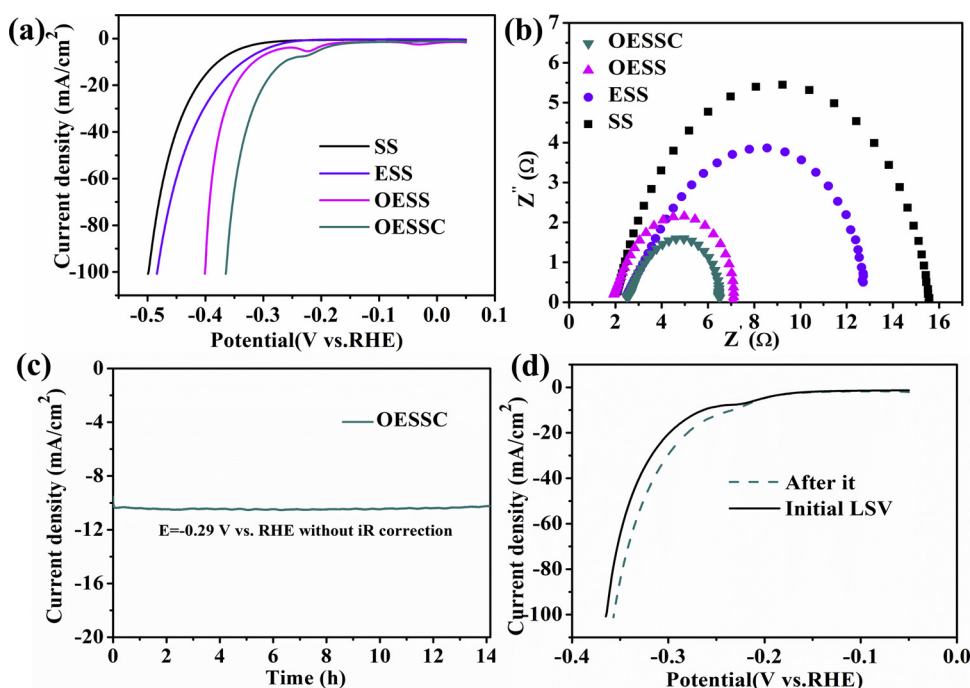
Table 1
Physicochemical parameters and TOF values of SS-based samples.

Sample	BET A_S (m^2/g)	TPR $_{Fe2O3 \rightarrow FeO}$ M_H (mmol/g)	M_{Fe2O3} (mmol/g)	M_{Fe3C} (mmol/g)	TOF
ESS	1.391	5.559×10^{-2}	5.559×10^{-2}	–	4.289×10^{-4}
OESS	1.291	9.514×10^{-2}	9.514×10^{-2}	–	2.582×10^{-4}
OESSC	2.489	9.107×10^{-2}	4.124×10^{-2}	3.593×10^{-2}	6.057×10^{-3}

by plasma working parameters (Fig. S11a–c). These results indicate that high power, suitable treatment time and moderate treatment temperature would promote the enhancement of HER performance. In addition, the samples with oxidation and carbonization processes (like OSSC and OESSC) showed better HER performance than other samples (Fig. S11d). This is in agreement with the previous work that the combination of metal oxide nanoparticles and Fe₃C@G core shell nanoparticles can provide more active sites for HER [32,33]. Furthermore, the OESSC sample showed a long-term and stable HER, as revealed in Fig. 5c. LSV curves of OESSC sample before and after 54,000 s electrolysis (Fig. 5d) kept almost the same value, further verifying the stability of OESSC electrocatalyst. These results indicate that defect-rich multi-graded carbon structural OESSC sample owns optimized electronic structure to efficiently implement electrocatalytic water splitting.

To further evaluate the electrocatalytic performance, the Faradaic efficiency of OESSC was calculated by the gas production and Eqs. (1) and (2). The volume of O₂ and H₂ for OESSC were detected by gas chromatography. The theoretical and experimental data of O₂ and H₂ production were shown in Fig. S12, which demonstrates that the ratio of H₂ production and O₂ production is close to 2. On basis of these results, the FE of OESSC electrode is over 98%, meaning a nearly complete conversion of electric energy to hydrogen. In addition, we further used the OESSC electrodes to simultaneously serve as the anode and cathode (OESSC//OESSC) for water splitting. As shown in Fig. S13, the overall water splitting voltage is 1.74 V at 10 mA cm⁻², which is lower than the SS electrodes as the anode and cathode (SS//SS). The operating strategy including etching, oxidizing and carbonizing was also implemented on other commercial stainless steel (e.g. 304 stainless steel) to consolidate its feasibility and universality, as shown in Fig. S14. In general, the facile and feasible route reported in this work can

efficiently improve the electrocatalytic water-splitting behaviors of commercial stainless steel.

3.3. Role of carbide (Fe₃C) on the surface of 316L-type stainless steel

Usually, the performance of the electrocatalyst is closely related to the quantity and species of the surface active sites. First of all, the specific surface area (A_s) was evaluated by the nitrogen adsorption-desorption isotherms and Brunauer-Emmett-Teller (BET) equation (shown in Table 1). The A_s of OESSC sample is almost twice than that of OESS sample and ESS sample, meaning more active sites exposed on the surface of OESSC. Further, the electrochemically active surface area of OESSC, OESS, ESS and SS samples were estimated by electrochemical double-layer capacitance (C_{dl}) (Figs. 6 and S15). It reveals that the C_{dl} of OESSC sample (~0.99 m F cm⁻²) is over three times higher than the OESS sample (~0.27 m F cm⁻²), which indicates that the CH₄ plasma treatment not only exfoliated the sample surface to active sites but also promoted to produce the Fe₃C@G composite nanoparticles on the sample surface as reactive sites. In addition, similar activation effects is also found in single process of CH₄ plasma treatment, as seen in Fig. S16. Combined with these results and sample characterization, the presence of the Fe₃C@G composite nanoparticles on the surface of OESSC sample can play an important role for accelerating the electrocatalytic water splitting.

To further assess the composition of active sites on the surface of OESSC sample, XPS depth analyses were performed to study the composition and chemical state of OESSC sample. The surface of OESSC sample had more C atoms than other elements due to the formation of the carbon layer (Fig. 7a). Meanwhile, compared to the signals of C and O, the signals of metal elements were hardly observed on the surface of
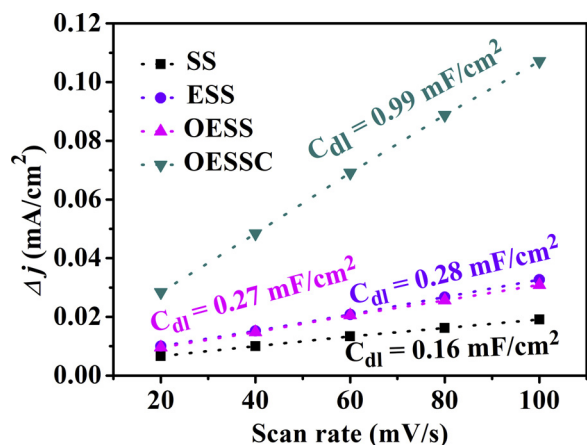
Fig. 6. C_{dl} values of SS-based samples determined by capacitive current at 1.175 V vs. RHE.

the OESSC sample. The XPS depth analysis of OESSC sample was performed at the range from 0 to 50 nm. As shown in Fig. 7b–d, the composition and chemical state of the surface for the OESSC sample had significantly changed with increasing the etching depth (d) from 0 to 10 nm. The C 1s peak can be deconvoluted into five peaks at 283.8, 284.8, 285.9, 286.9 and 287.9 eV, which could be attributed to iron carbide (Fe_3C), trigonal bonded carbon (sp^2 centers), tetrahedral bonded carbon (sp^3 centers), C−O group and C=O groups [29,30], respectively. It can be observed that the ratio of functional groups, like carbonyl (C=O) groups, on the surface ($d = 0$ nm) is higher than that in the inner (10 nm $\geq d > 0$ nm), resulting from the oxidation of amorphous carbon on the edge and "dangling bonds" in the ambient. Besides, the sample at 10 nm $\geq d > 0$ nm exhibits more Fe_3C than that at $d = 0$ nm. In addition, it is well known that carbon materials contain basal-plane sp^2 carbon atoms and defect sp^3 carbon atoms, and the defect level is usually reflected by the sp^3 content. The value of sp^2/sp^3 for OESSC sample decreases from 3.07 to 1.93 with the increase of the

etching depth from 0 nm to 10 nm (Fig. S17d), indicating more defects in the inner than on the surface. The O 1 s can be split into five peaks at 529.9 eV, 531.6 eV, 532.6 eV, 533.8 eV and 535 eV, which are assigned to metal-oxygen bonds, oxygen double bond to carbon (O=C−O), carbonyl (C=O) functional groups, oxygen single bond to carbon (O=C−O) and chemisorbed oxygen or water (H−O−H), respectively [14,29,34,35]. In Fig. 7c, the content of carbon-oxygen functional groups on the surface is much higher than inside the sample (10 nm $\geq d > 0$ nm), in line with the result of C 1s spectra. In addition, the increase of O=C−OH on the surface can be attributed to edge-dangling bonds of amorphous carbon structure absorbing the water or oxygen from the atmosphere. The Fe 2p3/2 peak contains Fe, Fe_3C, Fe^{2+} and Fe^{3+} centered at 706.8 eV, 708.2 eV, 710.3 eV and 712.3 eV, respectively. The Fe 2p3/2 spectra confirm that the inner of the sample at 10 nm $\geq d > 0$ nm has more low-valence-state Fe compounds than the sample surface because of the reducing action of CH_4 plasma treatment. Thus, we can image that the Fe atoms meet the charged C atoms to yield the Fe_3C during CH_4 plasma process [36]. In comparison to the sample at $d = 10$ nm, the sample at 50 nm $\geq d > 10$ nm shows the same chemical environment (Fig. S17a–d). Overall, after CH_4 plasma treatment, the amorphous carbon layer including carbide (Fe_3C), carbon-oxygen functional groups, edges and defects is formed in the OESSC sample, namely, the carbonization layer is obtained. It is reported that the amorphous carbon layer with more exposed edges, defects and functional groups (oxygen doping) can provide more active sites [32,33]. Furthermore, the $Fe_3C@G$ core shell nanoparticles can significantly improve activities and kinetics for four-electron transfer pathways, due to the modulation of electron density and electronic potential distribution at the neighboring graphene active sites by a penetration electron from Fe_3C core [37], which should be responsible for enhancing the water-splitting performance.

To further evaluate the modulation of electron density and electronic potential distribution by the $Fe_3C@G$ core shell nanoparticles on the surface of OESSC sample, the surface work function was analyzed using UPS technique. The UPS is highly sensitive to the change of surface electron state, and thus can detect the surface work function.
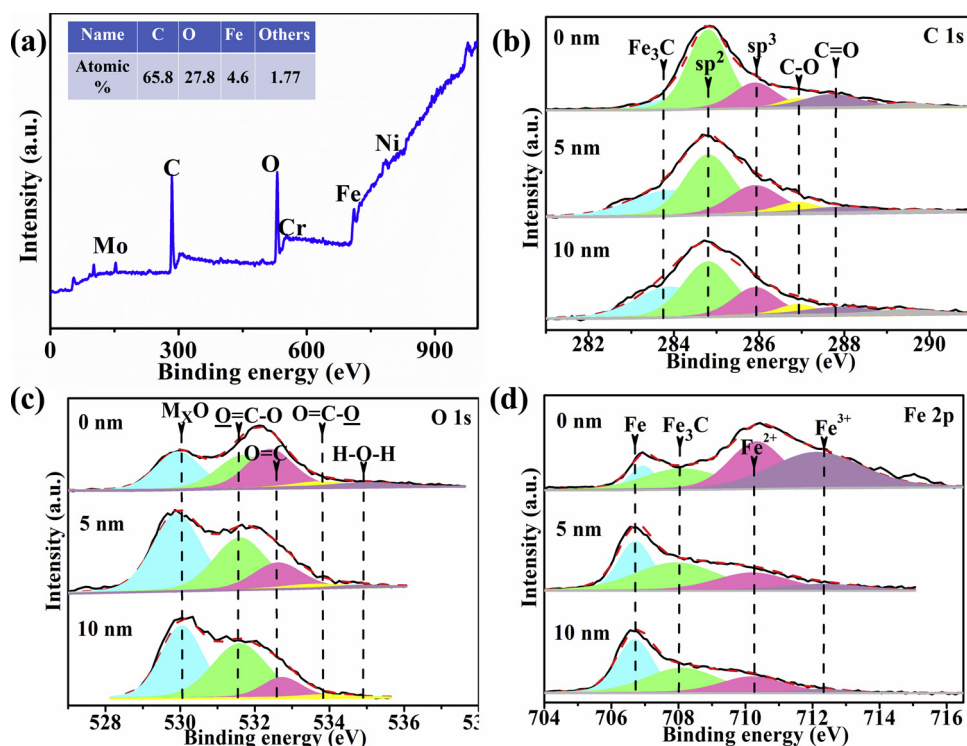

Fig. 7. (a) XPS survey spectrum of OESSC sample with $d = 0$ nm. High-resolution XPS depth analyses spectra of OESSC sample: (b) C 1s, (c) O 1s, and (d) Fe 2p3/2.
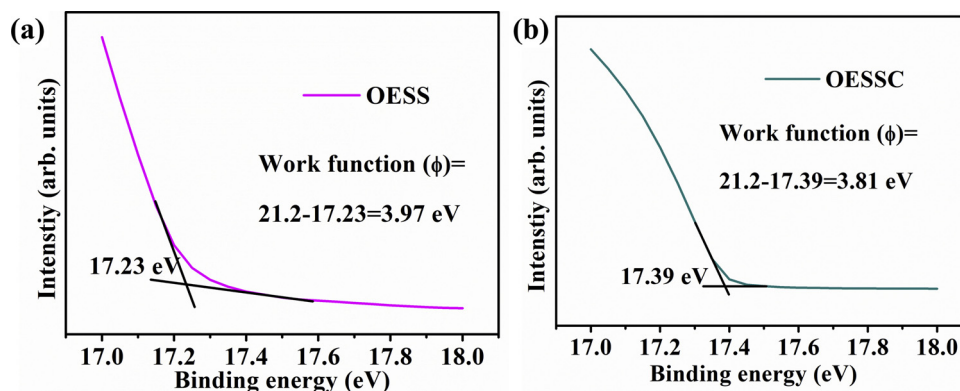
Fig. 8. UPS curves of (a) OESS sample and (b) OESS sample. According to the ultraviolet light (hν) of 21.2 eV, the work function (φ) of OESS and OESSC is 3.97 eV and 3.81 eV, respectively.

The work function of OESSC sample was 3.81 eV, which is lower than that of OESS sample (3.97 eV) (in Fig. 8). This result confirms that the Fe$_3$C@G core shell nanoparticles can modify the electron state on the surface. The low surface work function of OESSC sample is expected to carry out a high chemical reactive activity from the functionalized region of Fe$_3$C@G core shell, providing much faster electron transfer and the more active region for water splitting catalysis [38].

The amount of Fe$_3$C in the OESSC sample can be indirectly obtained by H$_2$-TPR technology, which was employed to determine the form and amount of the metal oxides on the surface of catalysts. As shown in Fig. S18, two separated peaks located at 370–500 °C and 600–900 °C can be found, which indicated the Fe$_2$O$_3$ → FeO and FeO → Fe reduction process by H$_2$, respectively [39,40]. It is easily observed that the reduction temperature of OESS sample is lower than the OESS sample, being attributed to the excitation of the iron oxide via the other substance, like iron carbide [41]. In addition, the TPR profiles reveal that Fe$_2$O$_3$ → FeO reduction process is easily occurred and take the majority of H$_2$ consumption. On basis of the H$_2$ consumption (M_{H_2} as shown in Table 1) in Fe$_2$O$_3$ → FeO process, we assume that all the Fe$_2$O$_3$ was decomposed to FeO by reduction process, the chemical equation as follows,

$$Fe_2O_3 + H_2 \rightarrow 2FeO + H_2O$$
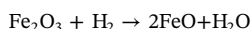
and thus the molar mass of Fe$_2$O$_3$ ($M_{Fe_2O_3} = M_{H_2}$, Table 1) could be acquired. Surprisingly, OESSC sample showed the lower H$_2$ consumption as well as less iron oxide on the surface than OESS, which is inconsistent with the increase of exposed surface area and active sites. Consequently, the Fe$_3$C@G composite nanoparticles replacing the iron oxide most possibly acts as the active reactive sites in OESSC sample. Meanwhile, in our experimental system, the content of Fe element per unit area exposed on the surface is identical in all the samples. The amount of Fe$_3$C is calculated by the Eq. (6), shown in Table 1

$$M_{Fe_3C} = \frac{2}{3}(M_{Fe_2O_3,OESS} - M_{Fe_2O_3,OESSC}) \tag{6}$$

where $M_{Fe_2O_3,OESS}$, M_{Fe_3C} and $M_{Fe_2O_3,OESSC}$ is the molar mass of Fe$_2$O$_3$ in OESS, molar mass of Fe$_3$C in OESSC, and molar mass of Fe$_2$O$_3$ in OESSC, respectively.

The turnover frequency (TOF) as a very important kinetic parameter for OER is calculated for evaluating the performance of the catalysts. According to the previous analysis, the active sites of OESSC sample should be the Fe$_3$C@G core shell nanoparticles. All the Fe atoms of the iron carbide are taken into account as active sites in OESSC sample. As summarized in Table 1, the TOF value of OESSC sample for OER is much higher than that of other samples. The combination of electrochemical performance and TOF values indicates that the formation of the Fe$_3$C@G core shell nanoparticles on the surface of OESSC sample can significantly improve the electrocatalytic activities.

4. Conclusion

In summary, we developed a simple and efficient strategy to in-situ evolved the active layer, consisting of amorphous carbon and graphene encapsulated Fe$_3$C nanoparticles, on the surface of 316L-type stainless steel as highly efficient electrocatalyst for OER. The CH$_4$ plasma treatment was used to realize the edges and defects, and carbide (Fe$_3$C) on the surface of 316L-type stainless steel. After treatment, the increase of active sites and the tuning of electronic properties made a significant contribution to enhancing the electrocatalytic performances of stainless steel-based electrodes for water splitting, especially OER. Finally, the optimized sample exhibited a high activity with an overpotential of only 290 mV at 10 mA cm^{-2} and an outstanding kinetics with the Tafel slope of 38 mV dec^{-1} for OER. This strategy provided an efficient, low-cost and high durable electrocatalysts for water splitting.

Acknowledgements

Appendix A. Supplementary data

Supplementary material related to this article can be found, in the online version, at doi:https://doi.org/10.1016/j.apcatb.2019.02.032.

References

[1] X. Fan, Y. Liu, S. Chen, J. Shi, J. Wang, A. Fan, W. Zan, S. Li, W.A. Goddard 3rd, X.M. Zhang, Defect-enriched iron fluoride-oxide nanoporous thin films bifunctional catalyst for water splitting, Nat. Commun. 9 (2018) 1809–1819.

[2] J.Y. Zheng, Y.H. Lyu, C. Xie, R.L. Wang, L. Tao, H.B. Wu, H.J. Zhou, S.P. Jiang, S.Y. Wang, Defect-enhanced charge separation and transfer within protection Layer/Semiconductor structure of photoanodes, Adv. Mater. 30 (2018) 1801773–1801779.

[3] J.Y. Zheng, Y.H. Lyu, R.L. Wang, C. Xie, H.J. Zhou, S.P. Jiang, S.Y. Wang, Crystalline TiO$_2$ protective layer with graded oxygen defects for efficient and stable silicon-based photocathode, Nat. Commun. 9 (2018) 3572–3581.

[4] J.Y. Zheng, S.H. Bao, X.L. Zhang, H.B. Wu, R.X. Chen, P. Jin, Pd-MgNi$_x$ nano-spheresiblack-TiO$_2$ porous films with highly efficient hydrogen production by near-complete suppression of surface recombination, Appl. Catal. B: Environ. 183 (2016) 69–74.

[5] Y. Liu, S. Jiang, S. Li, L. Zhou, Z. Li, J. Li, M. Shao, Interface engineering of (Ni, Fe) S$_2$@MoS$_2$ heterostructures for synergetic electrochemical water, Appl. Catal. B: Environ. 247 (2019) 107–114.

[6] W. Li, X. Gao, D. Xiong, F. Wei, W.-G. Song, J. Xu, L. Liu, Hydrothermal synthesis of monolithic Co$_3$Se$_4$ nanowire electrodes for oxygen evolution and overall water splitting with high efficiency and extraordinary catalytic stability, Adv. Energy Mater. 7 (2017) 1602579–1602585.

[7] B.K. Kim, S.K. Kim, S.K. Cho, J.J. Kim, Enhanced catalytic activity of electro-deposited Ni-Cu-P toward oxygen evolution reaction, Appl. Catal. B: Environ. 237 (2018) 409–415.

[8] H. Fan, H. Yu, Y. Zhang, Y. Zheng, Y. Luo, Z. Dai, B. Li, Y. Zong, Q. Yan, Fe-doped Ni$_3$C nanodots in N-Doped carbon nanosheets for efficient hydrogen-evolution and oxygen-evolution electrocatalysis, Angew. Chem. Int. Ed. Engl. 56 (2017) 12566–12570.

[9] S. Wan, J. Qi, W. Zhang, W. Wang, S. Zhang, K. Liu, H. Zheng, J. Sun, S. Wang, R. Cao, Hierarchical Co(OH)F superstructure built by low-dimensional sub-structures for electrocatalytic water oxidation, Adv. Mater. 29 (2017) 1700286–1700295.

[10] J. Liu, D. Zhu, T. Ling, A. Vasileff, S.-Z. Qiao, S-NiFe$_2$O$_4$ ultra-small nanoparticle built nanosheets for efficient water splitting in alkaline and neutral pH, Nano Energy 40 (2017) 264–273.

[11] L. Xu, Q. Jiang, Z. Xiao, X. Li, J. Huo, S. Wang, L. Dai, Plasma-engraved Co$_3$O$_4$ nanosheets with oxygen vacancies and high surface area for the oxygen evolution reaction, Angew. Chem. Int. Ed. Engl. 55 (2016) 5277–5281.

[12] Z.Q. Liu, H. Cheng, N. Li, T.Y. Ma, Y.Z. Su, ZnCo$_2$O$_4$ quantum dots anchored on nitrogen-doped carbon nanotubes as reversible oxygen reduction/evolution elec-trocatalysts, Adv. Mater. 28 (2016) 3777–3784.

[13] R. Xiang, Y. Duan, L. Peng, Y. Wang, C. Tong, L. Zhang, Z. Wei, Three-dimensional Core@Shell Co@CoMoO4 nanowire arrays as efficient alkaline hydrogen evolution electro-catalysts, Appl. Catal. B: Environ. 246 (2019) 41–49.

[14] Q. Che, Q. Li, Y. Tan, X. Chen, X. Xu, Y. Chen, One-step controllable synthesis of amorphous (Ni-Fe)S$_x$/NiFe(OH)$_y$ hollow microtube/sphere films as superior bi-functional electrocatalysts for quasi-industrial water splitting at large-current-den-sity, Appl. Catal. B: Environ. 246 (2019) 337–348.

[15] H. Schäfer, S.M. Beladi-Mousavi, L. Walder, J. Wollschläger, O. Kuschel, S. Ichilmann, S. Sadaf, M. Steinhart, K. Küpper, L. Schneider, Surface oxidation of stainless steel: oxygen evolution electrocatalysts with high catalytic activity, ACS Catal. 5 (2015) 2671–2680.

[16] F. Yu, F. Li, L. Sun, Stainless steel as an efficient electrocatalyst for water oxidation in alkaline solution, Int. J. Hydrogen Energy 41 (2016) 5230–5233.

[17] M.S. Balogun, W. Qiu, Y. Huang, H. Yang, R. Xu, W. Zhao, G.R. Li, H. Ji, Y. Tong, Cost-effective alkaline water electrolysis based on nitrogen- and phosphorus-doped self-supportive electrocatalysts, Adv. Mater 29 (2017) 1702095–1702105.

[18] H. Schäfer, D.M. Chevrier, P. Zhang, J. Stangl, K. Müller-Buschbaum, J.D. Hardege, K. Kuepper, J. Wollschläger, U. Krupp, S. Dühnen, M. Steinhart, L. Walder, S. Sadaf, M. Schmidt, Electro-oxidation of Ni42 steel: a highly active bifunctional electro-catalyst, Adv. Funct. Mater. 26 (2016) 6402–6417.

[19] H. Schäfer, M. Chatenet, Steel: the resurrection of a forgotten water-splitting cat-alyst, ACS Energy Lett. 3 (2018) 574–591.

[20] S. Hamann, I. Burlacov, H.J. Spies, H. Biermann, J. Ropcke, Spectroscopic in-vestigations of plasma nitriding processes: a comparative study using steel and carbon as active screen materials, J. Appl. Phys. 121 (2017) 153301–153309.

[21] H.A. Esquivel-Puentes, T.S. Fisher, G. Capote, J.J. Olaya, Bias effects on wear and corrosion behavior of amorphous hydrogenated carbon films with zirconia inter-layer, Surf. Coat. Technol. 350 (2018) 603–620.

[22] D. Deng, K.S. Novoselov, Q. Fu, N. Zheng, Z. Tian, X. Bao, Catalysis with two-dimensional materials and their heterostructures, Nat. Nanotechnol. 11 (2016) 218–230.

[23] J. Deng, P. Ren, D. Deng, X. Bao, Enhanced electron penetration through an ul-trathin graphene layer for highly efficient catalysis of the hydrogen evolution re-action, Angew. Chem. Int. Ed. Engl. 54 (2015) 2100–2104.

[24] J. Deng, P. Ren, D. Deng, L. Yu, F. Yang, X. Bao, Highly active and durable non-precious-metal catalysts encapsulated in carbon nanotubes for hydrogen evolution reaction, Energy Environ. Sci. 7 (2014) 1919–1923.

[25] J. Deng, L. Yu, D. Deng, X. Chen, F. Yang, X. Bao, Highly active reduction of oxygen on a FeCo alloy catalyst encapsulated in pod-like carbon nanotubes with fewer walls, J. Mater. Chem. A 1 (2013) 14868.

[26] C.C.L. McCrory, S.H. Jung, J.C. Peters, T.F. Jaramillo, Benchmarking heterogeneous electrocatalysts for the oxygen evolution reaction, J. Am. Chem. Soc. 135 (2013) 16977–16987.

[27] S.J. Li, D. Bao, M.M. Shi, B.R. Wulan, J.M. Yan, Q. Jiang, Amorphizing of Au na-noparticles by CeO$_x$-RGO hybrid support towards highly efficient electrocatalyst for N$_2$ reduction under ambient conditions, Adv. Mater. 29 (2017) 1700001–1700006.

[28] Y. Jia, L.Z. Zhang, A.J. Du, G.P. Gao, J. Chen, X.C. Yan, C.L. Brown, X.D. Yao, Defect graphene as a trifunctional catalyst for electrochemical reactions, Adv. Mater. 28 (2016) 9532–9538.

[29] Z.J. Liu, Z.H. Zhao, Y.Y. Wang, S. Dou, D.F. Yan, D.D. Liu, Z.H. Xia, S.Y. Wang, In situ exfoliated, edge-rich, oxygen-functionalized graphene from carbon fibers for oxygen electrocatalysis, Adv. Mater. 29 (2017) 1606207–1606213.

[30] L. Tao, Q. Wang, S. Dou, Z.L. Ma, J. Huo, S.Y. Wang, L.M. Dai, Edge-rich and do-pant-free graphene as a highly efficient metal-free electrocatalyst for the oxygen reduction reaction, Chem. Commun. 52 (2016) 2764–2767.

[31] X.G. Wang, D.S. Miller, E. Bukusoglu, J.J. de Pablo, N.L. Abbott, Topological defects in liquid crystals as templates for molecular self-assembly, Nat. Mater. 15 (2016) 106–112.

[32] S. Dou, A. Shen, L. Tao, S. Wang, Molecular doping of graphene as metal-free electrocatalyst for oxygen reduction reaction, Chem. Commun. (Camb) 50 (2014) 10672–10675.

[33] S. Dou, L. Tao, J. Huo, S. Wang, L. Dai, Etched and doped Co9S$_8$/graphene hybrid for oxygen electrocatalysis, Energy Environ. Sci. 9 (2016) 1320–1326.

[34] L.Z. Fan, S.Y. Qiao, W.L. Song, M. Wu, X.B. He, X.H. Qu, Effects of the functional groups on the electrochemical properties of ordered porous carbon for super-capacitors, Electrochim. Acta 105 (2013) 299–304.

[35] Z. Xiao, Y. Wang, Y.-C. Huang, Z. Wei, C.-L. Dong, J. Ma, S. Shen, Y. Li, S. Wang, Filling the oxygen vacancies in Co3O4 with phosphorus: an ultra-efficient electro-catalyst for overall water splitting, Energy Environ. Sci. 10 (2017) 2563–2569.

[36] Y.C. Wang, T. Zhou, K. Jiang, P.M. Da, Z. Peng, J. Tang, B.A. Kong, W.B. Cai, Z.Q. Yang, G.F. Zheng, Reduced mesoporous Co$_3$O$_4$ nanowires as efficient water oxidation electrocatalysts and supercapacitor electrodes, Adv. Energy Mater. 4 (2014) 1400696–1400712.

[37] W.J. Jiang, L. Gu, L. Li, Y. Zhang, X. Zhang, L.J. Zhang, J.Q. Wang, J.S. Hu, Z.D. Wei, L.J. Wan, Understanding the high activity of Fe-N-C electrocatalysts in oxygen reduction: Fe/Fe3C nanoparticles boost the activity of Fe-N-x, J. Am. Chem. Soc. 138 (2016) 3570–3578.

[38] D.H. Deng, L. Yu, X.Q. Chen, G.X. Wang, L. Jin, X.L. Pan, J. Deng, G.Q. Sun, X.H. Bao, Iron encapsulated within pod-like carbon nanotubes for oxygen reduction reaction, Angew. Chem. Int. Ed. Engl. 52 (2013) 371–375.

[39] L. Zhou, L.R. Enakonda, S. Li, D. Gary, P. Del-Gallo, C. Mennemann, J.M. Basset, Iron ore catalysts for methane decomposition to make CO$_x$ free hydrogen and carbon nano material, J. Taiwan Inst. Chem. E 87 (2018) 54–63.

[40] L. Zhou, L.R. Enakonda, M. Harb, Y. Saih, A. Aguilar-Tapia, S. Ould-Chikh, J.L. Hazemann, J. Li, N. Wei, D. Gary, P. Del-Gallo, J.M. Basset, Fe catalysts for methane decomposition to produce hydrogen and carbon nano materials, Appl. Catal. B: Environ. 208 (2017) 44–59.

[41] X.F. Tang, Y.G. Li, X.M. Huang, Y.D. Xu, H.Q. Zhu, J.G. Wang, W.J. Shen, MnOx-CeO2 mixed oxide catalysts for complete oxidation of formaldehyde: effect of preparation method and calcination temperature, Appl. Catal. B: Environ. 62 (2006) 265–273.